Chinese Chemical Letters 34 (2023) 107824

Contents lists available at ScienceDirect

Chinese Chemical Letters

journal homepage: www.elsevier.com/locate/cclet

Highly dispersed L1$_2$-Pt$_3$Fe intermetallic particles supported on single atom Fe-N$_x$-C$_y$ active sites for enhanced activity and durability towards oxygen reduction

Tuo Zhao[a,b], Yang Li[a,b], Jie Liu[a,b], Xian Wang[a,b], Jiayi Zhang[c], Changpeng Liu[a,b], Wei Xing[a,b], Junjie Ge[a,b,*]

[a] *State Key Laboratory of Electroanalytical Chemistry, Jilin Province Key Laboratory of Low Carbon Chemical Power, Changchun Institute of Applied Chemistry, Chinese Academy of Sciences, Changchun 130022, China*
[b] *School of Applied Chemistry and Engineering, University of Science and Technology of China, Hefei 230026, China*
[c] *Fuyuan British American School, Shenzhen 518126, China*

ARTICLE INFO

Article history:
Received 7 June 2022
Revised 22 August 2022
Accepted 12 September 2022
Available online 15 September 2022

Keywords:
Intermetallic alloys
Single atom active sites
ORR
Synergistic effect
Confinement effect

ABSTRACT

Highly active and durable oxygen reduction reaction (ORR) catalysts with sufficient activity and stability of Pt are beneficial for the commercialization of proton exchange membrane fuel cells. Here we report an effective approach to prepare a composite catalyst comprising of ordered L1$_2$-Pt$_3$Fe intermetallic nanoparticles interact with single atom Fe-N$_x$-C$_y$ active sites. The addition of Fe and the confinement effect of hierarchical porous structure limit the growth of intermetallic particle size (around 2.5 nm). The ligand effect of the electron transfer from Fe to Pt and the synergistic interaction between L1$_2$-Pt$_3$Fe and Fe-N$_x$-C$_y$ work together to reduce oxygen intermediates adsorption and improve kinetics process. Experimentally, the L1$_2$-Pt$_3$Fe/C$_{\text{Fe-N-C}}$ catalyst shows high mass activity and specific activity at 1.010 A/mg$_{\text{Pt}}$ and 1.166 mA/cm^2, respectively, which are 5.8 and 5.1 times higher than those of commercial Pt/C (0.174 A/mg$_{\text{Pt}}$ and 0.230 mA/cm^2). Thanks to the more stable L1$_2$ structure, L1$_2$-Pt$_3$Fe/C$_{\text{Fe-N-C}}$ exhibits better durability (14 mV $E_{1/2}$ loss of L1$_2$-Pt$_3$Fe/C$_{\text{Fe-N-C}}$ and 33 mV $E_{1/2}$ loss of commercial Pt/C) after 30,000 cycles accelerated stress tests. The strategy to design and prepare small particle Pt-based intermetallic alloys coordinated with M-N-C active sites provides a new direction to obtain low-cost and easily prepared effective ORR catalysts.

The advantages of superb energy efficiency, high power density and environmental sustainability make proton exchange membrane fuel cells (PEMFCs) the promising power sources for new energy vehicles to alleviate environmental pollution and energy crisis [1,2]. However, fuel cells with the sluggish kinetics of the oxygen reduction reaction (ORR) at the cathode require more precious metal Pt catalysts to achieve desired power density [3,4]. Two negative factors limit the application of Pt-based catalysts: on one hand, the high price of Pt increases the overall cost of fuel cells; on the other hand, the dissolution and agglomeration of Pt particles cause rapid power decay during fuel cell operation. To address these pressing issues, it is desirable to improve the utilization and the stability of Pt [5].

The oxygen binding energy of Pt is 0.2 eV lower than the optimal value in volcano plot [6]. Due to the smaller atomic radius and lower electronegativity, incorporating transition metals in Pt can regulate electronic structure and lattice strain, Pt alloys therefore exhibit more appropriate d-band center and enhanced ORR activity. Many researchers have reported that Pt alloys like Pt$_x$Ni$_y$, Pt$_x$Co$_y$, Pt$_x$Fe$_y$, *etc.* show superior mass activity and intrinsic activity during the past decades [7–9]. Alloys can be divided into disordered solid solutions and intermetallic compounds. Intermetallic compound with regular atomic arrangement can reduce the dissolution of Pt and transition metal, this atomic structure advantage makes Pt intermetallics exhibit enhanced stability in durability tests [8,10]. However, high temperature treatment is a necessary procedure for the formation of intermetallic and nanoparticle agglomeration easily occurs during this stage, which will reduce

---

[*] Corresponding author at: State Key Laboratory of Electroanalytical Chemistry, Jilin Province Key Laboratory of Low Carbon Chemical Power, Changchun Institute of Applied Chemistry, Chinese Academy of Sciences, Changchun 130022, China.
E-mail address: gejj@ciac.ac.cn (J. Ge).

https://doi.org/10.1016/j.cclet.2022.107824

electrochemically active surface areas (ECSAs) for high mass activity [11]. Hence, developing an effective strategy to prepare Pt-based intermetallic catalysts meanwhile maintaining sufficiently fine particle sizes remains a huge challenge.

Support materials play a significant role in improving the activity and stability because of their high conductivity, electrochemical stability and specific surface area [12]. A pity is that the conventional carbon supports are inactive so the big surface area cannot be fully utilized by active sites. Fortunately, the synergistic effect between Pt-based particles and M-N-C has been innovatively found in recent progress [13–15]. However, the formation of Pt_xM_y alloys often damages the already existing M-N-C active sites and the preparation methods are often complex and difficult to get the final catalysts [16], which drives us to explore effective ways to prepare easily available catalysts with better coordination between Pt-based alloy and M-N-C active sites. The most active M-N-C catalysts are atomically dispersed Fe-N-C catalyst derived from zeolitic imidazolate framework-8 (ZIF-8) precursors [17]. The nitrogen species and micropores are also abundant in ZIF-8, which are favorable for the dispersion and anchoring of Pt. The strong metal-support interaction from N doping can improve the adhesion strength between Pt particles and support, reducing the support corrosion and Pt migration [18]. Therefore, Pt particles are expected to be highly dispersed on the surface of Fe-N-C meanwhile the synergistic effect between Pt alloys and Fe-N-C single-atom active sites are beneficial for ORR activity and stability.

Here, we report our progress of the highly active and robust $L1_2$-$Pt_3Fe/C_{Fe\text{-}N\text{-}C}$ ORR catalyst in 0.1 mol/L $HClO_4$ comprised of ordered $L1_2$-Pt_3Fe intermetallic particles supported on single atom Fe-N-C active sites derived from ZIF-8. We improved the ORR performance through synergistic catalysis between $L1_2$-Pt_3Fe intermetallic and Fe-N-C. Specifically, the uniform and fine $L1_2$-Pt_3Fe particles can retain a desirable particle size (around 2.5 nm) on the Fe-N-C support after heat treatment. The alloying effect of Fe can reduce activation energy to break O-O bonds and the hierarchical porous of ZIF-8 can be fully utilized by single atom Fe-N-C active sites. The as-prepared $L1_2$-$Pt_3Fe/C_{Fe\text{-}N\text{-}C}$ exhibits outstanding ORR activity (half-wave potential of 0.932 V and mass activity of 1.010 A/mg_{Pt}) and great durability after 30,000 cycles (14 mV loss of $E_{1/2}$ and 0.587 A/mg_{Pt} retained of mass activity).

In the typical synthesis of $C_{N\text{-}C}$, $Zn(NO_3)_2{\cdot}6H_2O$ (3.0 g) is dissolved in 40 mL of methanol with stirring, then 2-methylimidazole (6.5 g) in 80 mL of methanol is poured into above solution followed by vigorous stirring for 24 h at room temperature. The as-obtained product is centrifuged and washed with ethanol several times and finally dried overnight in oven at 50 °C. Then the ZIF-8 precursor is heat-treated at 950 °C for 2 h under Ar/H_2 (gas flow ratio is 90/10). The resulting powder is leached by 1 mol/L HCl at room temperature for 12 h to obtain the final $C_{N\text{-}C}$. In the typical synthesis of $C_{Fe\text{-}N\text{-}C}$, the difference is that $Zn(NO_3)_2{\cdot}6H_2O$ (3.0 g) and $Fe(acac)_3$ (660 mg) are dissolved together in 40 mL of methanol, other steps are unchanged.

For the synthesis of $L1_2$-$Pt_3Fe/C_{N\text{-}C}$ and $L1_2$-$Pt_3Fe/C_{Fe\text{-}N\text{-}C}$, 30 mg $C_{N\text{-}C}$ and $C_{Fe\text{-}N\text{-}C}$ are dispersed in 40 mL ethanol and ultrasonic 30 min. Then 3.6 mg Pt (1.5 mg_{Pt}/mL, H_2PtCl_6 solution, self-configured) and 0.33 mg Fe (1.5 mg_{Fe}/mL, $FeCl_3$ solution, self-configured) are poured into above solution and stirred 12 h. The precursors obtained by rotary evaporation are heat-treated at 700 °C for 2 h under Ar/H_2 (gas flow ratio is 90/10). The resulting powders are leached by 0.5 mol/L HNO_3 at room temperature for 12 h to obtain the final $L1_2$-$Pt_3Fe/C_{N\text{-}C}$ and $L1_2$-$Pt_3Fe/C_{Fe\text{-}N\text{-}C}$.

In the typical synthesis of $Pt/C_{N\text{-}C}$ and $Pt/C_{Fe\text{-}N\text{-}C}$, the difference is that only 3.6 mg Pt (1.5 mg_{Pt}/mL, H_2PtCl_6 solution, self-configured) is poured into support solution, other steps are unchanged.

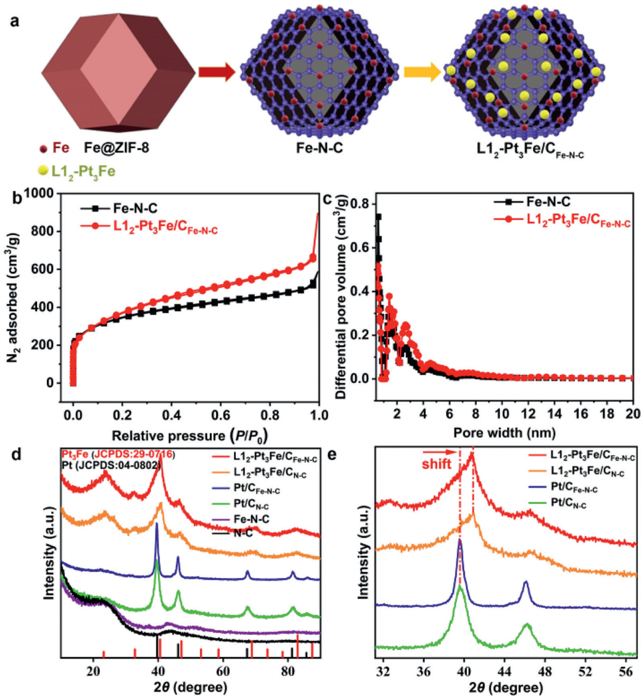

Fig. 1. (a) synthetic procedures for $L1_2$-$Pt_3Fe/C_{Fe\text{-}N\text{-}C}$. (b) Nitrogen adsorption-desorption isotherms of $L1_2$-$Pt_3Fe/C_{Fe\text{-}N\text{-}C}$ and Fe-N-C. (c) Pore size distribution of $L1_2$-$Pt_3Fe/C_{Fe\text{-}N\text{-}C}$ and Fe-N-C. (d) XRD patterns of different catalysts. (e) The shift of Pt (111) to big angle in XRD pattern.

As shown in Fig. 1a, we prepared the Fe-N-C support with highly active Fe-N_x-C_y by the pyrolysis of Fe@ZIF-8. Fe^{3+} can replace Zn^{2+} to coordinate with 2-methylimidazole during the self-assembly process of ZIF-8 [19], then the Fe-N-C support can be obtained by pyrolyzing the ZIF-8 nanocrystal precursors doped Fe^{3+}. The Fe-N-C substrate with hierarchical porous structures and strong metal-support interaction can adsorb Pt and Fe ions easily and uniformly on surface. The final catalyst $L1_2$-$Pt_3Fe/C_{Fe\text{-}N\text{-}C}$ is acquired by the second annealing treatment, which results in alloying Pt and Fe to form ordered $L1_2$-Pt_3Fe intermetallic structure. It is worth mentioning that we try to add urea to reduce the loss of Fe-N-C active sites in the secondary pyrolysis process. For comparison, NC is prepared by ZIF-8 without Fe^{3+} doped. $L1_2$-$Pt_3Fe/C_{N\text{-}C}$ is prepared by synthesizing Pt_3Fe nanoparticles on the N-C substrate. As for the $Pt/C_{Fe\text{-}N\text{-}C}$ and $Pt/C_{N\text{-}C}$, they were prepared by synthesizing the Pt particles on the Fe-N-C and N-C substrates, respectively.

Then we evaluated the specific surface area and porous structure by the N_2 adsorption/desorption isothermal physisorption curves and DFT pore size distribution plots [20]. Fe-N-C and $L1_2$-$Pt_3Fe/C_{Fe\text{-}N\text{-}C}$ all show a type IV isotherm, meanwhile the specific surface area is 1232 m^2/g and 1339 m^2/g, respectively (Fig. 1b). The dramatic increase of Fe-N-C and $L1_2$-$Pt_3Fe/C_{Fe\text{-}N\text{-}C}$ in low P/P_0 region suggests the existence of a lot of micropores, the higher nitrogen adsorption of $L1_2$-$Pt_3Fe/C_{Fe\text{-}N\text{-}C}$ at medium relative pressure indicates that $L1_2$-$Pt_3Fe/C_{Fe\text{-}N\text{-}C}$ has more mesopores than Fe-N-C. These isothermal physisorption curves are interpreted more clearly by DFT pore size distribution plots: $L1_2$-$Pt_3Fe/C_{Fe\text{-}N\text{-}C}$ and Fe-N-C have similar pore size distribution with a large number of micropores while $L1_2$-$Pt_3Fe/C_{Fe\text{-}N\text{-}C}$ has more mesopores around 2.5 nm (Fig. 1c). These high specific surface areas and abundant pore structure are beneficial for both anchoring the metal particles and accelerating mass transfer process during ORR reaction [21].

In Fig. 1d, after pyrolyzing the ZIF-8 precursor with or without Fe, the diffraction peaks of Fe-N-C and N-C at 25° and 44° represent the (002) and (001) of graphitized-C and no obvious crys-

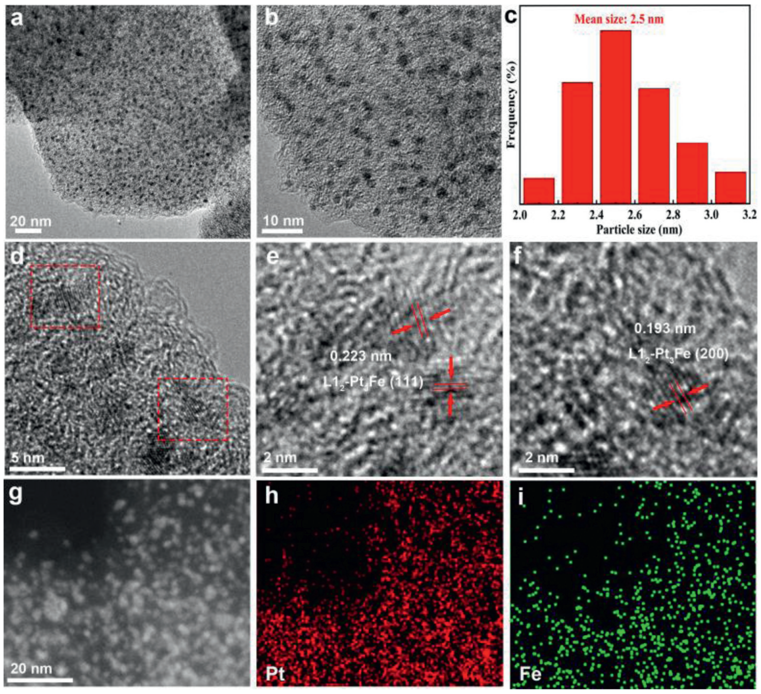

Fig. 2. (a, b) TEM images of L1$_2$-Pt$_3$Fe/C$_{\text{Fe-N-C}}$. (c) Particle size of L1$_2$-Pt$_3$Fe/C$_{\text{Fe-N-C}}$. (d-f) HRTEM images and lattice fringes of L1$_2$-Pt$_3$Fe/C$_{\text{Fe-N-C}}$. (g-i) EDS-elemental mappings of Pt and Fe.

talline peaks appear in the XRD patterns, excluding the presence of metal particles in the Fe-N-C and N-C. We adsorbed H_2PtCl_6 on Fe-N-C and N-C and then heated treated them to obtain Pt/C$_{\text{Fe-N-C}}$ and Pt/C$_{\text{N-C}}$. XRD patterns display four diffraction peaks located at 39.76°, 46.24°, 67.45° and 81.28°, respectively, corresponding to the (111), (200), (220) and (311) planes of Pt (JCPDS No. 04–0802), which proves that we successfully prepared Pt particles on Fe-N-C and N-C. Compared with Pt/C$_{\text{Fe-N-C}}$ and Pt/C$_{\text{N-C}}$, we adsorbed H_2PtCl_6 and $FeCl_3$ together on Fe-N-C and N-C to prepare L1$_2$-Pt$_3$Fe/C$_{\text{Fe-N-C}}$ and L1$_2$-Pt$_3$Fe/C$_{\text{N-C}}$, we can observe distinctly different diffraction peaks in XRD patterns [22]: the XRD patterns of L1$_2$-Pt$_3$Fe/C$_{\text{Fe-N-C}}$ and L1$_2$-Pt$_3$Fe/C$_{\text{N-C}}$ agree well with the intermetallic L1$_2$-Pt$_3$Fe (JCPDS No. 29–0716), demonstrating the formation of ordered L1$_2$-Pt$_3$Fe intermetallic structure. Super lattice peaks at 23.08° and 47.02° can be assigned to (100) and (200) planes of L1$_2$-Pt$_3$Fe [23]. Meanwhile, the (111) characteristic peak becomes more smooth and broader along with the introduction of Fe, implying the decrease in particle size according to Scherrer Formula. More importantly, the position of highly active crystal face (111) shifts to the high angle (Fig. 1e), indicating that the successful introduction of small atomic radius Fe results in a significant compression of the Pt lattice [24]. We know that the strain effect is beneficial for weakening O_2/intermediates adsorption and thus improves intrinsic ORR activity.

In order to study the L1$_2$-Pt$_3$Fe/C$_{\text{Fe-N-C}}$ morphology and active site structure information, high-resolution TEM (HRTEM) was applied. Fe particles were not found in Fe-N-C (Fig. S1 in Supporting information), showing that Fe exists in the form of Fe-N$_x$-C$_y$ single atoms. We observed evident particle aggregation in Pt/C$_{\text{Fe-N-C}}$ and Pt/C$_{\text{N-C}}$ (Figs. S2 and S3 in Supporting information). Specifically, the particle size distribution is extremely uneven and the diameter of some particles can even reach tens of nanometers. Although we succeeded in finding the characteristic lattice fringes of Pt (111), we know that there is still a long way to prepare a kind of high-performance ORR catalyst. Luckily, the particle sizes of L1$_2$-Pt$_3$Fe/C$_{\text{Fe-N-C}}$ and L1$_2$-Pt$_3$Fe/C$_{\text{N-C}}$ are considerably reduced, especially the particle diameter of L1$_2$-Pt$_3$Fe/C$_{\text{Fe-N-C}}$ is concentrated at around 2.5 nm meanwhile particles are highly dispersed on the support (Figs. 2a-c and Fig. S4 in Supporting information). We are encouraged by the reported literature that 2.5 nm is close to the optimum particle size of Pt for ORR reaction [25]. This change is easily obtainable that the presence of Fe during nucleation is helpful for the reduction of particle size, which is consistent with the L1$_2$-Pt$_3$Fe/C$_{\text{Fe-N-C}}$ XRD results of smooth and broad diffraction peaks. Interestingly, the particle size of L1$_2$-Pt$_3$Fe/C$_{\text{Fe-N-C}}$ is in good correlation with mainly mesopore size (both around 2.5 nm), we thus deduce that the particle size is limited by the confinement effect of hierarchical pore. The presence of lattice fringes at 0.223 and 0.195 nm are clearly observed, corresponding to the (111) and (200) facet of the L1$_2$-Pt$_3$Fe intermetallic structure (Figs. 2d-f). There is a 1.3% compressive strain of Pt (111) compared with Pt/CF$_{\text{e-N-C}}$ and Pt/C$_{\text{N-C}}$, and this lattice shrinkage is in accordance with the peak shift to high angle observed in XRD. The elements of Pt and Fe are uniformly distributed on the support by scanning transmission electron microscopy energy dispersive spectrometer (STEM-EDS) elemental mapping (Figs. 2g-i), and the similar distribution of Pt and Fe reveals the alloying feature of the two elements. In summary, the TEM images and XRD patterns are in good agreement, which more clearly shows that 2.5 nm L1$_2$-Pt$_3$Fe particles are highly dispersed on support and the alloying Fe compresses the lattice of Pt.

X-ray photoelectron spectroscopy (XPS) was used to investigate the electronic structure of L1$_2$-Pt$_3$Fe/C$_{\text{Fe-N-C}}$ and Fe-N-C. Compared with the Pt/C, L1$_2$-Pt$_3$Fe/C$_{\text{Fe-N-C}}$ displays a 0.3 eV negative shift to lower binding energy (Fig. 3a). This electronic change can shift d-band center downward and weaken reaction intermediates adsorption, thus intensifying d-orbital overlapping and optimizing binding strength [26]. The Fe 2p$_{3/2}$ and 2p$_{1/2}$ peaks of Fe-N-C are indistinct due to low Fe content on the surface (Fig. 3b), the Fe 2p spectra of L1$_2$-Pt$_3$Fe/C$_{\text{Fe-N-C}}$ depicts two main peaks at 710.6 eV of 2p$_{3/2}$ and 724.3 eV of 2p$_{1/2}$, which can be assigned to Fe^{3+} [27]. We know Fe and Pt have been bonded strongly in the form of L1$_2$-Pt$_3$Fe, and Fe donates electrons to Pt because of the lower electronegativity than Pt, causing the high valence state of Fe^{3+} and

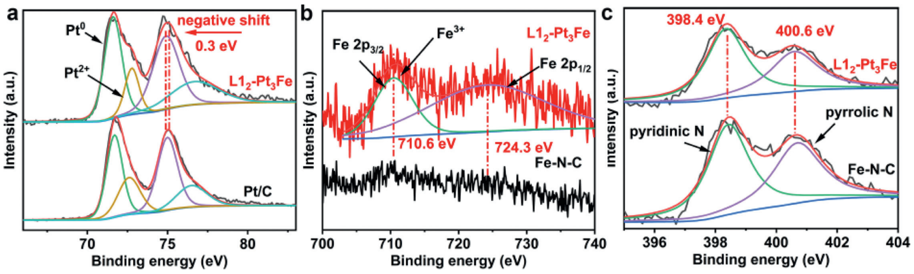

Fig. 3. (a) Pt 4f spectra of $L1_2$-$Pt_3Fe/C_{Fe\text{-}N\text{-}C}$ and Pt/C. (b) Fe 2p spectra of $L1_2$-$Pt_3Fe/C_{Fe\text{-}N\text{-}C}$ and Fe-N-C. (c) N 1s spectra of $L1_2$-$Pt_3Fe/C_{Fe\text{-}N\text{-}C}$ and Fe-N-C.

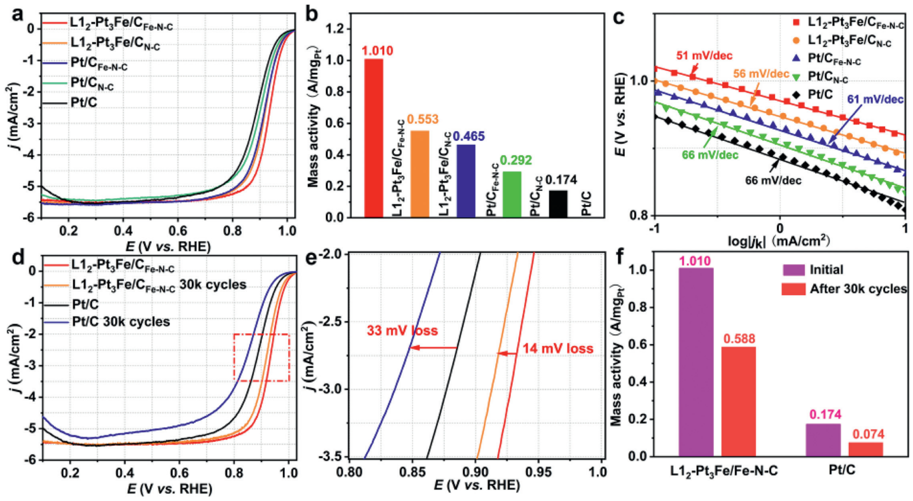

Fig. 4. (a) LSVs of different catalysts. (b) Mass activity of different catalysts. (c) Tafel slope of different catalysts. (d) LSVs of $L1_2$-$Pt_3Fe/C_{Fe\text{-}N\text{-}C}$ and Pt/C before and after ADTs. (e) LSVs loss of $L1_2$-$Pt_3Fe/C_{Fe\text{-}N\text{-}C}$ and Pt/C. (f) Mass activity loss of $L1_2$-$Pt_3Fe/C_{Fe\text{-}N\text{-}C}$ and Pt/C.

negative shift of Pt. The N 1s spectra for $L1_2$-$Pt_3Fe/C_{Fe\text{-}N\text{-}C}$ and Fe-N-C are similar (Fig. 3c): The peaks located at 398.4 eV and 400.6 eV are pyridinic N and pyrrolic N, respectively, the total N content is increased from 5.28 wt% to 5.83 wt% and pyridine N accounts for most of N content (Table S1 in Supporting information) [28], implying that Fe-N-C active sites do not decrease after the second heat treatment. Inductively coupled plasma optical emission spectrometer (ICP-OES) results support the deduction from other side: Fe-N-C exhibits mass fraction of Fe at 0.64 wt% and meanwhile the Fe and Pt contents of $L1_2$-$Pt_3Fe/C_{Fe\text{-}N\text{-}C}$ are 1.88 wt% and 12.6 wt%, respectively (Table S2 in Supporting information). Subtracting the amount of Fe in form of Fe-N-C from the total Fe content, the remaining Fe and Pt are converted to an atomic ratio, the ratio is approximately 1:3, which is consistent with the theoretical atomic ratio in $L1_2$-Pt_3Fe. These N species not only provide plentiful ligands to anchor metal atoms but also modify local electronic structure of Fe-N-C for high ORR activity. All in all, the electron transfer from Fe to Pt downshifts the Pt d-band center, optimizing the binding affinity between Pt and oxygen intermediates. On the other side, the formation of $L1_2$-Pt_3Fe does not damage the previous Fe-N-C active sites. We have sufficient reasons to expect the synergy effect between $L1_2$-Pt_3Fe and Fe-N-C toward effective ORR reaction.

The ORR activity of $L1_2$-$Pt_3Fe/C_{Fe\text{-}N\text{-}C}$, $L1_2$-$Pt_3Fe/C_{N\text{-}C}$, $Pt/C_{Fe\text{-}N\text{-}C}$, $Pt/C_{N\text{-}C}$ and Fe-N-C were compared in 0.1 mol/L $HClO_4$ solution by the rotating disk electrode (RDE). We firstly evaluated the ORR performance of Fe-N-C compared with commercial Pt/C: the electrical double layer of Fe-N-C is much bigger than Pt/C and the half wave potential $E_{1/2}$ of Fe-N-C is 0.820 V, demonstrating that Fe-N-C is a promising Pt-based catalyst support (Fig. S5 in Supporting information). Then a series of Pt-based catalysts were synthesized after metal adsorption and pyrolysis. ORR performance of Pt-based catalysts is significantly improved: The half-wave potentials of $L1_2$-$Pt_3Fe/C_{Fe\text{-}N\text{-}C}$, $L1_2$-$Pt_3Fe/C_{N\text{-}C}$, $Pt/C_{Fe\text{-}N\text{-}C}$ and $Pt/C_{N\text{-}C}$ show 0.932 V, 0.917 V, 0.913 V, 0.898 V, respectively, compared with commercial Pt/C 0.883 V (Fig. 4a). The mass activity at 0.9 V *vs.* RHE are calculated to estimate the ORR intrinsic activity: $L1_2$-$Pt_3Fe/C_{Fe\text{-}N\text{-}C}$ shows the highest mass activity of 1.010 A/mg$_{Pt}$ compared with $L1_2$-$Pt_3Fe/C_{N\text{-}C}$, $Pt/C_{Fe\text{-}N\text{-}C}$, $Pt/C_{N\text{-}C}$ and Pt/C (0.553 A/mg$_{Pt}$, 0.465 A/mg$_{Pt}$, 0.292 A/mg$_{Pt}$, and 0.174 A/mg$_{Pt}$) (Fig. 4b). In addition to the obviously alloying effect to improve ORR performance ($L1_2$-Pt_3Fe shows better ORR activity than Pt), we can clearly observe that not only Pt_3Fe intermetallic but also Pt particles supported on Fe-N-C show significantly improved ORR activity than the same particles supported on N-C. This elevation can also be verified from the Tafel slope calculation (Fig. 4c): Pt_3Fe intermetallic and Pt particles loaded on Fe-N-C (51 mV/dec and 61 mV/dec) show lower Tafel slopes than these loaded on N-C (56 mV/dec and 66 mV/dec). We can conclude that the synergistic effect between $L1_2$-Pt_3Fe intermetallic particles and Fe-N-C can improve the kinetics process and the activity for ORR [29].

To further explore the reason why $L1_2$-$Pt_3Fe/C_{Fe\text{-}N\text{-}C}$ exhibits such high activity, we calculated the electrochemically active surface area (ECSA) compared with commercial Pt/C. The ECSA is usually measured by the hydrogen underpotential deposition (Hupd) method, but the Hupd of $L1_2$-$Pt_3Fe/C_{Fe\text{-}N\text{-}C}$ is partially covered due to the big electrical double layer [30], so we evaluated the more realistic ECSA by CO stripping (Fig. S6 in Supporting information). The ECSA of $L1_2$-$Pt_3Fe/C_{Fe\text{-}N\text{-}C}$ (86.6 m^2/g) is bigger than commercial Pt/C (75.5 m^2/g), the large ECSA derived from uniform and small particle size is beneficial for the interaction with oxygen intermediate species. Then we calculate the specific activity

(SA) from the obtained MA and ECSA, the SA of $L1_2$-$Pt_3Fe/C_{Fe\text{-}N\text{-}C}$ (1.166 mA/cm^2) is 5.1 times higher than Pt/C (0.230 mA/cm^2). Finally, we used accelerated durability tests (ADTs) to measure the stability of $L1_2$-$Pt_3Fe/C_{Fe\text{-}N\text{-}C}$ and commercial Pt/C for 30,000 cycles between 0.6 V and 1.0 V in O_2-saturated 0.1 mol/L $HClO_4$ solution (Figs. 4d and e). $L1_2$-$Pt_3Fe/C_{Fe\text{-}N\text{-}C}$ exhibits much high durability (14 mV half-wave potential loss) compared with Pt/C (33 mV half-wave potential loss). The mass activity (Fig. 4f) of $L1_2$-$Pt_3Fe/C_{Fe\text{-}N\text{-}C}$ retains 58.2% (0.588 A/mg$_{Pt}$) after the ADTs while Pt/C only retains 43% (0.075 A/mg$_{Pt}$). The electrochemical tests show that the synergistic effect between $L1_2$-Pt_3Fe intermetallic alloy and Fe-N-C can greatly increase ORR activity meanwhile $L1_2$-$Pt_3Fe/C_{Fe\text{-}N\text{-}C}$ performs excellent durability after the ADTs.

In summary, we designed and successfully prepared $L1_2$-Pt_3Fe intermetallic alloy supported on single atom Fe-N-C active sites, which performs enhanced ORR activity (initial half-wave potential of 0.932 V) and durability (14 mV $E_{1/2}$ loss after 30,000 cycles) compared with commercial Pt/C (0.883 V of $E_{1/2}$ and 33 mV $E_{1/2}$ loss). The incorporation of Fe and the porous morphology are beneficial for the highly dispersed $L1_2$-Pt_3Fe particles with small size (2.5 nm). The alloying effect weakens the adsorption of oxygen intermediate species and the synergistic effect between $L1_2$-Pt_3Fe and Fe-N-C improves the kinetics process. These two effects work together to improve ORR activity. The simple and effective method to synthesize $L1_2$-$Pt_3Fe/C_{Fe\text{-}N\text{-}C}$ will open a new avenue to the better cooperation between Pt-based intermetallic particles and single atom M-N-C active sites. Moreover, the approach to achieve ordered intermetallic alloy with a small particle size (around 2.5 nm) will provide a new idea for preparing intermetallic compounds that resist particle agglomeration.

Declaration of competing interest

The authors declare that they have no conflict of interest.

Acknowledgments

The work was supported by the National Science and Technology Major Project (No. 2017YFB0102900), National Natural Science Foundation of China (Nos. 21633008, 21673221 and U1601211), Jilin Province Science and Technology Development Program (Nos. 20200201001JC, 20190201270JC and 20180101030JC).

Supplementary materials

Supplementary material associated with this article can be found, in the online version, at doi:10.1016/j.cclet.2022.107824.

References

[1] S. Zaman, L. Huang, A.I. Douka, et al., Angew. Chem. Int. Ed. 60 (2021) 17832–17852.
[2] T. Zhao, E. Luo, X. Wang, et al., J. Electrochem. 26 (2020) 84–95.
[3] L.L. Chen, X.L. Xu, W.X. Yang, et al., Chin. Chem. Lett. 31 (2020) 626–634.
[4] T. Zhao, E.G. Luo, Y. Li, et al., Sci. China Mater. 64 (2021) 1671–1678.
[5] J. Wang, W. Ding, Z.D. Wei, Acta Chim. Sin. 37 (9) (2021) 2009094.
[6] X.F. Zhu, X. Tan, K.H. Wu, et al., Angew. Chem. Int. Ed. 60 (2021) 21911–21917.
[7] G.M. Leteba, Y.C. Wang, T.J.A. Slater, et al., Nano Lett. 21 (2021) 3989–3996.
[8] X. Li, Y.H. He, S.B. Cheng, et al., Adv. Mater. 33 (2021) 2106371.
[9] W. Li, D.D. Wang, T.Y. Liu, et al., Adv. Funct. Mater. 32 (2022) 2109244.
[10] P. Gao, M. Pu, Q.J. Chen, et al., Catalysts 11 (2021) 1050.
[11] Z.N. Lin, A.Z. Yang, B.B. Zhang, et al., Adv. Funct. Mater. 32 (2022) 2107683.
[12] J.R.C. Salgado, F. Alcaide, G. Alvarez, et al., J. Power Sources 195 (2010) 4022–4029.
[13] J. Ma, B. Liu, R.Y. Wang, et al., Chin. Chem. Lett. 33 (2022) 2585–2589.
[14] Z. Qiao, C.Y. Wang, C.Z. Li, et al., Energy Environ. Sci. 14 (2021) 4948–4960.
[15] L. Chong, J.G. Wen, J. Kubal, et al., Science 362 (2018) 1276–1281.
[16] X. Ao, W. Zhang, B.T. Zhao, et al., Energy Environ. Sci. 13 (2020) 3032–3040.
[17] R.Q. Zhong, C.X. Zhi, Y.X. Wu, et al., Chin. Chem. Lett. 31 (2020) 1588–1592.
[18] S. Zaman, Y.Q. Su, C.L. Dong, et al., Angew. Chem. Int. Ed. 61 (2022) e202115835.
[19] H.G. Zhang, H.T. Chung, D.A. Cullen, et al., Energy Environ. Sci. 12 (2019) 2548.
[20] P. Guo, B. Liu, Y.K. Dai, et al., J. Colloid Interface Sci. 613 (2022) 276–284.
[21] E.G. Luo, Y.Y. Chu, J. Liu, et al., Energy Environ. Sci. 14 (2021) 2158–2185.
[22] A. Tomou, I. Panagiotopoulos, V. Tzitzios, et al., J. Magn. Magn. Mater. 334 (2013) 107–110.
[23] N. Cheng, L. Zhang, S.Y. Mi, et al., ACS Appl. Mater. Interfaces 10 (2018) 38015–38023.
[24] X.X. Wang, S. Hwang, Y.T. Pan, et al., Nano Lett. 18 (2018) 4163–4171.
[25] T. Asset, R. Chattot, M. Fontana, et al., ChemPhysChem 19 (2018) 1552–1567.
[26] J.R. Li, Z. Xi, Y.T. Pan, et al., J. Am. Chem. Soc. 140 (2018) 2926–2932.
[27] E.G. Luo, C. Wang, Y. Li, et al., Nano Res. 13 (2020) 2420–2426.
[28] S.N. Zhao, J.K. Li, R. Wang, et al., Adv. Mater. 34 (2022) 2107291.
[29] X.M. Ge, A. Sumboja, D. Wuu, et al., ACS Catal. 5 (2015) 4643–4667.
[30] X.L. Tian, X. Zhao, Y.Q. Su, et al., Science 366 (2019) 850–856.